Inflow Velocity and Rotational Effects on Revolving and Translating Wings

James H Paulson, Thierry Jardin, James H J Buchholz

https://doi.org/10.1063/5.0171240

Inflow-velocity and rotational effects on revolving and translating wings

James H. Paulson,[1] Thierry Jardin,[2] and James H. J. Buchholz[1,a)]

AFFILIATIONS

[1]Department of Mechanical Engineering and IIHR–Hydroscience and Engineering, University of Iowa, Iowa City, Iowa 52242, USA
[2]Institut Supérieur de l'Aéronautique et de l'Espace (ISAE-Supaero), Université de Toulouse, Toulouse 31055, Cedex 4, France

[a)]Author to whom correspondence should be addressed: james-h-buchholz@uiowa.edu

ABSTRACT

An aspect ratio 9.5 rectangular wing is articulated in revolving and translating motions at a 45° angle of incidence and Reynolds number $Re = O(300)$. The effects of rotational (Coriolis and centripetal) accelerations and relative inflow velocity profile on vorticity transport within the leading-edge vortex (LEV) system are independently investigated. For the range of displacements studied (180° rotation and corresponding translational displacement), a stably attached leading-edge vortex (LEV) is observed when rotational accelerations and/or a linearly varying inflow velocity profile is present; however, the inflow velocity profile has a stronger effect on stability of the LEV. LEV vorticity magnitude and lift are significantly augmented when both factors are included (i.e., the full revolving wing case). Vorticity transport analyses are conducted in a planar control region two chords from the axis of rotation, where LEV stability is typically observed on revolving wings at high incidence and at an equivalent spanwise position in the translating case. The fully revolving wing case exhibits a substantially larger leading-edge shear-layer vorticity flux than the other cases, whereas Coriolis tilting makes little contribution to regulation of LEV strength. A correlation is found between the spanwise convective flux and tilting flux contributions in all cases. Decomposition of the spanwise convective flux term demonstrates that the two phenomena are kinematically linked and, together, define a new out-of-plane convective flux term that captures the essence of the spanwise convective flux. The role of this term and the effect of rotational accelerations on it are examined.

I. INTRODUCTION

It is well established that revolving, rolling, or flapping of wings or blades can have a profound effect on the development of stall and the evolution of the leading-edge vortex (LEV) in a broad range of natural and engineered systems, such as aircraft propellers and rotors, wind turbines, gas turbine blades, and biological or bio-inspired fliers.[1–5] On high-angle-of-attack aerodynamic structures, rotational effects can stabilize leading-edge vortices (LEVs), often resulting in higher sectional lift coefficients and greater force stability than similar translating wings.[5,6] At a given spanwise location, we define unstable LEVs as those in which the vortex core is advected downstream, and ceases to interact with the wing, and stable LEVs as those which remain in proximity to the wing and perpetually influence the sectional aerodynamic loads. This stabilizing effect is known to be governed by each of the two primary attributes distinguishing rotating and translating wings: non-inertial accelerations in the rotating frame of reference and spanwise variation of the relative inflow velocity.[7] However, it is not well understood how these two attributes affect transport of vorticity within the LEV, which regulates the strength of the vortex system and thereby may influence its stability on the lifting surface. A better understanding of the relationships between rotational effects, transport processes, and aerodynamic consequences will support the development of reduced order models,[8] the optimization of blade shape, and the design of flow control strategies to optimize aerodynamic performance.[9,10] Furthermore, such a fundamental understanding of the underlying physics of vortex stability may inspire new design strategies for translating wings that are more robust to unsteady flow phenomena such as gusts.

The present study seeks to further elucidate the flow physics governing LEV evolution on rotating bodies by independently investigating the effects of the inflow velocity gradient and non-inertial accelerations on flow evolution, sectional lift performance, and vorticity transport. In particular, we seek to better understand to what extent these rotational effects influence the attachment of the vortex through the spanwise draining of vorticity from the LEV.[11,12] To achieve the comparison, we investigate two rotating cases and two translating cases. In each category, one case incorporates a uniform inflow velocity and the other, a linearly varying inflow velocity. A vorticity transport

framework is employed to help quantify the growth of the vortex system and to elucidate the influences of the rotation attributes.

II. BACKGROUND

The source of increased sectional lift for revolving wings has been attributed to multiple unsteady phenomena; however, a primary contributor is the LEV, as summarized in the reviews by Eldredge and Jones[5] and Chen *et al.*[13] Ford and Babinsky[14] demonstrated that, for an impulsively started translating wing, the LEV contained the majority of the total circulation about the wing. Also looking at impulsively started translating wings, Jardin *et al.*[15] empirically related the sectional lift coefficient with LEV circulation and the proximity of the LEV to the wing surface.

Biological flyers have been a primary inspiration for studies of LEV behavior. Lentink and Dickinson[3] visualized the flow field over a model fruit fly wing and demonstrated LEV dependence on rotational motion where LEV stability was attributed to rotational accelerations. This was further elucidated by the same authors,[16] who used theoretical analysis and flow visualizations to argue that both Coriolis and centripetal accelerations are important. Likewise, the centripetal acceleration number and the Rossby number (representing Coriolis accelerations) were shown to be relevant to a variety of flapping and spinning wing scenarios. Sufficiently small local Rossby numbers—proportional to spanwise distance from the rotation axis—were found to create suitable conditions for LEV stability, such that the LEV is more stable close to the root of a revolving wing. Lentink and Dickinson[16] proposed that spanwise flow on the wing, caused by centripetal acceleration, results in an upstream Coriolis acceleration, which stabilizes the vortex. However, Garmann *et al.*[17] computed a Coriolis force within the fluid over a revolving wing of aspect ratio one and demonstrated that the wing-normal component actually pointed *away* from the wing, promoting detachment.

Jardin[18] provided further insight into the role of Coriolis acceleration on LEV stability for an aspect ratio 9.5 rectangular wing, on which a stable LEV was observed over the inboard region at $Re \in [100, 750]$ (where the Reynolds number is based on the wing chord and midspan velocity). By artificially increasing the relative contribution of the Coriolis term in the Navier–Stokes equation, Jardin[18] was able to move the LEV instability point further outboard; however, at Reynolds numbers below 200, it was shown that Reynolds number more strongly influenced LEV stability. It was additionally noted that greater Coriolis accelerations increased spanwise flow within the LEV core, supporting the claim that spanwise flow promotes LEV attachment. Jardin and Colonius[19] used a numerical simulation to demonstrate that local Rossby numbers could be utilized to predict the salient flow features over a revolving wing, where lower Rossby numbers near the root of the wing promoted a stably attached LEV as the Coriolis effects dominate. Additionally, the root effects were studied by varying root cutoffs, where increasing the radial position of the wing root led to a conical LEV structure near the root even at Rossby numbers that demonstrated LEV detachment with smaller root cutoff.

The effect of inflow shear profile on LEV behavior was numerically studied by Jardin and David,[7] in which a rectangular planform wing was simulated with and without an inflow velocity gradient present. It was shown that the spanwise inflow gradient, viscous effects, and rotational accelerations (in the case of a revolving wing) all contributed to LEV attachment at low Reynolds numbers ($Re \approx 100$). Spanwise flow was enhanced by the presence of the inflow velocity gradient, and it was suggested that the spanwise inflow gradient was solely sufficient to sustain LEV attachment over small flapping amplitudes (i.e., up to approximately $\theta = 120°$). However, it did not significantly alter the lift coefficient of the wing in comparison with pure translation.

Stability of the LEV has often been understood, in part, as the result of transport phenomena, which act to limit the growth of the vortex, and thus prevent it from shedding after reaching a threshold size. Spanwise convection of vorticity in the core of the vortex has been postulated as one of these limiting mechanisms, in which the spanwise flow drains circulation from the vortex, through the tip vortex and into the wake.[11,12,20,21] However, spanwise gradients in LEV circulation must also be present for the phenomenon to be effective.[22] For example, Wong *et al.*[23] showed that spanwise flow could strengthen or weaken the vortex depending on the sign of the spanwise vorticity gradient. Jia *et al.* found that spanwise bending altered the spanwise convective flux (SPCF) such as to delay LEV growth.[10]

Nevertheless, spanwise transport of vorticity does not appear to be ubiquitous on revolving wings, nor necessary to maintain attachment of the leading-edge vortex. For example, Birch and Dickinson[24] found that blocking spanwise flow by applying chordwise fences to a revolving wing had little effect on vortex development. Chen *et al.*[25] investigated the starting rotation of an aspect ratio 4 wing at $Re = 1500$ and observed that spanwise convection of vorticity was only significant relatively early in the rotation and suggested that it may not be important for steadily revolving wings. Eldredge and Jones[5] derived a vorticity transport budget from which the spanwise convective flux vanishes identically. Other studies[26,27] found that the influence of spanwise convective flux on vortex circulation is often unimportant.

Derivation of a comprehensive vorticity transport budget provides a means of tracking not only the role of spanwise flow on vortex circulation (if any), but also identifies other sources and sinks of circulation governing its growth or decay. Such analyses typically reveal a significant role of the diffusive vorticity flux from solid surfaces due to pressure gradients, which typically leads to entrainment and cross-cancellation with the primary vortex.[28,29] Acharya and Metwally[30] showed, experimentally, that the diffusive flux is primarily active near the leading edge on a pitching airfoil. This interaction can have a substantial effect on the strength of the LEV. Shih and Ho[31] used an order-of-magnitude vorticity transport analysis to show that the diffusive contributions are on the same order of magnitude as the convective contributions during the formation of a dynamic stall vortex on an unsteady airfoil. More recent measurements of leading-edge vortices on lifting surfaces have quantitatively verified this assertion.[26–28,32] For example, Panah *et al.*[28] found the secondary vorticity flux on a plunging plate to be approximately half that of the leading-edge shear-layer flux.

From their own analyses and a review of the literature, Eldredge and Jones[5] concluded that interaction with the surface, as well as tilting of vorticity, is the primary means of vortex weakening, leading to the stabilization of leading-edge vortices on revolving wings. Specifically, they noted that the rotational motion of the wing induces a component of vorticity parallel to the rotation axis (as observed from an inertial coordinate system) that is tilted into the spanwise direction by the radial shear flow. This mechanism, which they dubbed *Coriolis tilting*, resulted in spanwise vorticity opposite to that in the LEV, thus weakening it. Werner *et al.*[33] verified the process through numerical

simulations and attributed the tilting to a vertical gradient of Coriolis acceleration. In contrast, Wabick *et al.*[34] found the Coriolis tilting contribution to be negligible on a wing rolling in a uniform flow, in comparison with other mechanisms of vorticity transport.

This study seeks to further elucidate the role of inflow velocity profile and rotational accelerations on leading-edge vortex development by invoking a vorticity transport framework developed by Wabick *et al.*[34] to understand how these two factors influence the fluxes of vorticity that govern the strength of the vortex system. A rectangular planform wing of aspect ratio $AR = 9.5$ is articulated in rotational and translational motions to isolate the effects of rotational accelerations, and inflow velocity gradients are systematically introduced to isolate their specific effects on LEV behavior. The large aspect ratio is used to mitigate tip effects. The case configurations are described in Sec. III, and details of the numerical scheme are given in Sec. IV. The vorticity transport analysis, which is described in Sec. V, is conducted in a plane located two chord lengths from the axis of rotation in the rotating cases—or 1.5 chord lengths from the wing root—and, correspondingly, 1.5 chord lengths from one end of the translating wings, due to the prominence of rotational effects within a few chord lengths of the rotation axis. A Reynolds number of 300 at the interrogation plane is investigated, which is relevant to small biological swimmers and flyers, and minimizes computational complexity while remaining sufficiently large to exhibit rotational effects that are robust through much larger Reynolds numbers.[18] To provide context for the analysis, the structures of the global flow fields and the spanwise vorticity and velocity fields are first presented in Sec. VI A, and sectional lift coefficients are discussed in Sec. VI B. The modes of vorticity transport for each of the cases are quantified and discussed in Sec. VI C. Motivated by observations of symmetry in the transport modes, a new form of the vorticity transport equation is introduced in Sec. VI D, leading to a new interpretation of the spanwise convective and tilting vorticity transport terms. In Sec. VI E, the four cases are reexamined in the context of the new vorticity transport terms identified in Sec. VI D.

III. PROBLEM SETUP

Four cases are considered with varied aspects of rotational motion, as summarized in Fig. 1. In all cases, the wing is held stationary in the domain and rotational effects are systematically introduced by including or excluding Coriolis and centripetal accelerations in the Navier–Stokes equations and incorporating either a uniform or linearly varying inflow velocity profile, as illustrated in Figs. 1(c) and 1(d). Two cases (A and C) are studied in a cylindrical domain [Fig. 1(a)] with azimuthal flow and Coriolis and centripetal accelerations included in the Navier–Stokes equations. The other two cases (B and D) are studied in a rectangular domain [Fig. 1(b)] with no rotational accelerations.

Case A, therefore, represents purely rotational motion, with an approach velocity that varies linearly with the distance from the axis of rotation and rotational accelerations included within the Navier–Stokes equations. Case B implements the same inflow velocity profile on the translating wing (where there are no Coriolis and centripetal accelerations). Cases C and D mirror cases A and B except that the inflow velocity is uniform along the span. Therefore, case D represents true translation of the wing in a quiescent fluid, and cases B and C are hybrid cases.

A rectangular planform wing of aspect ratio $AR = 9.5$ was simulated in each case. In the rotating-wing cases, the wing revolved about an axis perpendicular to the span and intersected the mid-chord. A root cutout of $0.5c$ (where c is the chord length of the wing) was used, resulting in a wing tip trajectory radius of $R = 10c$. The wing thickness is $0.04c$, with sharp leading and trailing edges.

The wing was impulsively started and rotated through a revolution angle of $\theta = 180°$, at a pitch angle of $\alpha = 45°$, far exceeding the

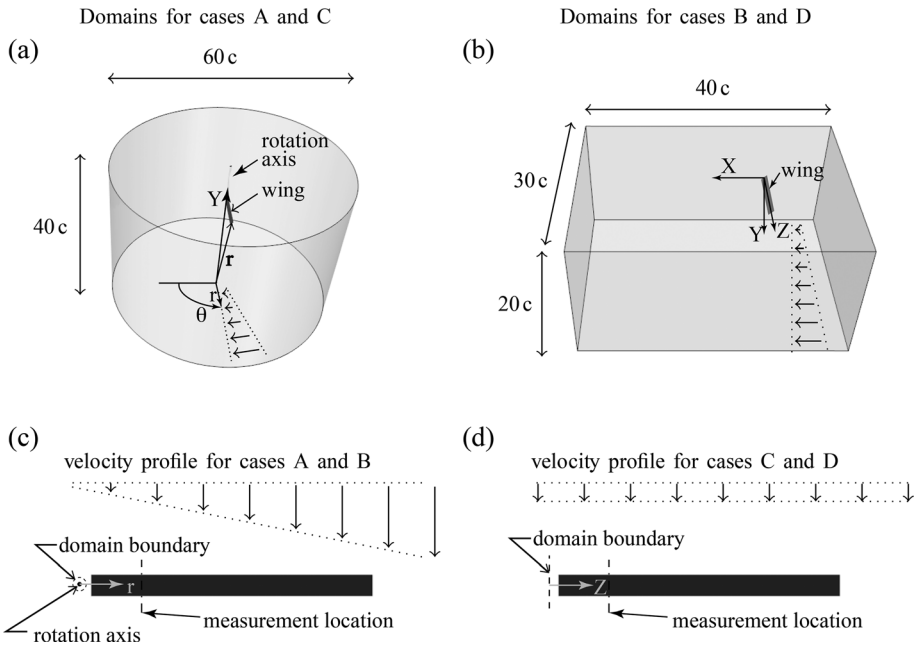

FIG. 1. The computational domains, inflow velocity profiles, and coordinate definitions: (a) Annular domain for cases A and C; (b) rectangular domain for cases B and D; (c) wing detail for cases A and C illustrated with the linearly varying inflow velocity profile applied to cases A and B; and (d) wing detail for cases B and D illustrated with the uniform inflow velocity profile applied to cases C and D.

TABLE I. Wing displacement correspondence, expressed in terms of azimuthal displacement θ (rotating wing) and tangential displacement δ (rotating and translating wings).

θ (deg)	5	30	60	90	120	180
δ	0.175	1.05	2.09	3.14	4.19	6.28

stall angle for the corresponding 2D wing. Most of the analyses in this study were conducted at a radial location of $r/c = 2$ (where r is the distance from the rotation axis and c is the wing chord), where prior studies have shown that rotational effects are strong, resulting in a locally attached LEV. The non-dimensional displacement of the wing, δ, is normalized by the wing chord. In the rotating cases, the displacement is measured at $r/c = 2$ such that $\delta = \theta r/c = \theta(2c)/c = 2\theta$ (rad.). The corresponding values of δ and angular displacement, θ, for rotating wings are presented in Table I.

The two translational cases were defined such as to match the inflow velocity at $r/c = 2$ of the rotating cases, as well as the inflow velocity gradient and angle of attack. Thus, the cases with uniform and linearly varying inflow velocity profiles have the inflow velocities matched at 1.5 chord lengths from the wing root (i.e., the end of the wing near the domain boundary), such that the chord-based Reynolds number is $Re_{c(r/c=2)} = 300$.

In the rotating cases, a global cylindrical coordinate system is defined with the Y axis coincident with the rotation axis, r in the radial direction, and θ in the azimuthal direction, as illustrated in Fig. 1(a). In the subsequent discussion, θ is used to characterize the progression of wing rotation. The vector $\mathbf{r}$, shown in Fig. 1, denotes position in the domain. The domain is annular with an inner radius of $0.25c$ to avoid discontinuity in the flow field in case C (which would exist at the rotation axis for a more conventional right circular cylinder shape). The wing maneuvers are simulated by holding the wing stationary and subjecting it to a circumferential velocity field with either a uniform or linearly varying velocity profile u_θ (i.e., $u_\theta = U$ or $u_\theta = \Omega r$, where U is the constant inflow velocity and $\Omega = 15.67$ rad/s is the equivalent wing rotation rate).

In the translating cases, a global rectangular coordinate system is defined, with the wing oriented along the Z axis and inflow velocity in the positive X direction, as illustrated in Fig. 1(b). Again the wing is held stationary and subjected to the same inflow profiles as for the revolving cases. The root of the translating wing is located $0.5c$ away from the sidewall of the domain to match the $0.5c$ root cutout in the revolving case. We further note that the spanwise Z direction in the rectangular domain corresponds to the radial direction (r) in the annular domain such that the extent of both domains in the spanwise directions is consistent (with a length equal to $30c$). For short simulation times as those considered here (i.e., shorter than a rotation period), the wake in cases A and C mainly advects in the azimuthal direction, while it advects in the positive X direction in cases B and D. Because θ is not bounded, there is no direct correspondence between the extent of the circular domain in the azimuthal direction and that of the rectangular domain in the X direction. For very large simulation times, the wake in cases A and C would advect in both the azimuthal and negative Y directions due to the vertical induced downwash. Accordingly, the extent of the circular domain in the Y direction is set to be consistent with that of the rectangular domain in the X direction (with a length equal to $40c$ in both domains). However, we stress that the dimensions of the domains are set such that the results do not depend on the location of the far-field boundary conditions.

Although cases B and C are hybrid rotating/translating cases that can be used to elucidate the individual effects of rotational accelerations and inflow velocity profile on flow structure, aerodynamics, and vorticity transport, it is important to note that case C contains additional artifacts. Specifically, the circumferential motion of the flow within the domain, with uniform azimuthal velocity profile, results in the radial pressure distribution shown in Fig. 2, in contrast to cases A, B, and D, in which the pressure is uniform in undisturbed regions of the domain. The theoretical pressure distribution shown in Fig. 2 is a solution to the Navier–Stokes equation in the cylindrical domain with the prescribed azimuthal velocity field. It should be noted that the pressure gradient within the wing tip radius ($r/c = 10$) is small, increasing further outboard. For case C at $r/c = 2.0$, the spanwise pressure gradient induced within the LEV generally exceeds the radial pressure gradient by two orders of magnitude. Second, the uniform azimuthal flow field $u_\theta = U$ is rotational, resulting in the background vorticity field $\omega_{Z,BG}$

$$\omega_{Z,BG} = \frac{1}{r}\frac{\partial(ru_\theta)}{\partial r} - \frac{1}{r}\frac{\partial u_r}{\partial \theta} = \frac{u_\theta}{r} = \frac{U}{r}. \tag{1}$$

The background vorticity is 125.4 rad/s at the domain inner boundary and drops to 62.7 rad/s at the wing root and 3.13 rad/s at the wing tip. It is 15.7 rad/s at $r/c = 2$, where most of the analysis is conducted in this paper. In contrast, the peak vorticity value over the wing is on the order of 800 rad/s at $r/c = 2$. The background vorticity for the true revolving wing (case A) is constant: $\omega_{Z,BG} = 2\Omega$.

IV. NUMERICAL SCHEME

The flow is computed by directly resolving the three-dimensional incompressible Navier–Stokes equations on annular and rectangular domains shown in Fig. 1. For cases A and C where the annular domain is used, the equations are solved in the non-inertial reference frame of

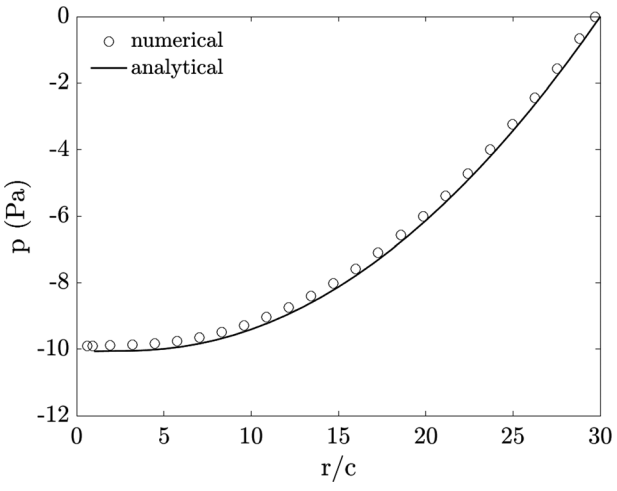

FIG. 2. Radial pressure distribution in case C. The analytical solution for uniform azimuthal velocity $u_\theta = U$ is $p(r) = \rho(U^2 ln(r) + \frac{\Omega^2 r^2}{2} + 2\Omega U r) + C$.

the wing where the Coriolis ($2\boldsymbol{\Omega} \times \boldsymbol{u}$) and centrifugal ($\boldsymbol{\Omega} \times (\boldsymbol{\Omega} \times \mathbf{r})$) terms apply and hence read

$$\frac{\partial \mathbf{u}}{\partial t} + \mathbf{u} \cdot \nabla \mathbf{u} = -\frac{1}{\rho}\nabla p - \boldsymbol{\Omega} \times (\boldsymbol{\Omega} \times \boldsymbol{r}) - 2\boldsymbol{\Omega} \times \mathbf{u} + \nu \nabla^2 \mathbf{u}. \quad (2)$$

In Eq. (2), t is the time, Ω is the wing rotation rate, and the variables u, p, ρ, and ν are the fluid velocity, pressure, density, and kinematic viscosity, respectively. For cases A and C, centripetal and Coriolis accelerations were computed using the rotation rate, Ω. For cases B and D where the rectangular domain is used, the Coriolis and centrifugal terms do not apply.

A cell-centered finite volume method (StarCCM+ v13.04) is used to solve the momentum and continuity equations in an uncoupled way, using a predictor-corrector approach. A variable arrangement and a Rhie-Chow-type pressure–velocity coupling combined with a SIMPLE-type algorithm are employed. Second-order schemes are used for both spatial and temporal discretizations. The numerical method is further detailed in the works by Demirdžić and Muzaferija.[35,36]

The annular domain has an outer diameter of $60c$ and height of $40c$, spatially discretized into 25×10^6 Cartesian cells. The cells are trimmed to fit the wing and the far field boundary surfaces. The typical grid spacing in all three dimensions and in the vicinity and wake of the wing is equal to $0.02c$. Specifically, the refined wake region extends approximately $6c$, $1.2c$, and 90° in the radial, vertical, and azimuthal direction, respectively, beyond which the grid spacing progressively relaxes to $1c$ at the far-field. The far-field boundary condition (including the inner surface of the annular domain) is treated as a Dirichlet velocity condition and the wing is modeled as a fixed, no-slip surface. The far-field condition, combined with the initial velocity condition, effectively enforces the incoming velocity to be that shown in Fig. 1. The wing motion is temporally discretized into 360 time steps.

The rectangular domain has a length of $40c$, a width of $30c$, and a height of $20c$. It is discretized into 26×10^6 Cartesian cells with similar grid spacings as used for the annular domain. Here, the refined wake region extends $6c$, $1.2c$, and $13.5c$ in the spanwise, vertical, and streamwise directions, respectively. Again, the far-field and the wing are treated as Dirichlet velocity condition and fixed, no-slip surface, respectively. The wing motion is temporally discretized into 360 time steps.

Figure 3(a) displays the sectional lift coefficient c_l as a function of δ obtained in case A at $r/c = 2$ (i.e., radial location considered throughout the paper) for three different typical grid spacings with $\Delta x = 0.01c$ (190×10^6 cells), $0.02c$ (25×10^6 cells), and $0.04c$ (3×10^6 cells). While large differences exist between the coarse ($0.04c$) and base ($0.02c$) size grids, base and fine ($0.01c$) size grids yield similar results, with differences on the mean lift and maximum differences on the instantaneous lift below 1% and 1.5%, respectively. Figure 3(b) displays spanwise vorticity isolines (non-dimensional value equal to -10) obtained for the three grids. Again, base and fine size grids are found to yield very similar flow topology. Figure 3(c) depicts the topology of the homogeneous hexahedral mesh around and in the wake of the wing for $\Delta x = 0.01c$, together with spanwise vorticity contours. Moreover, increasing the temporal resolution of the base size grid by a factor of 2 (i.e., from 360 to 720 time steps to discretize the motion) did not significantly change the results, with differences on the mean lift and maximum differences on the instantaneous lift below 0.1% and 0.5%, respectively.

Finally, for completeness, results obtained using the present approach are compared with those from Ref. 17 for an aspect ratio

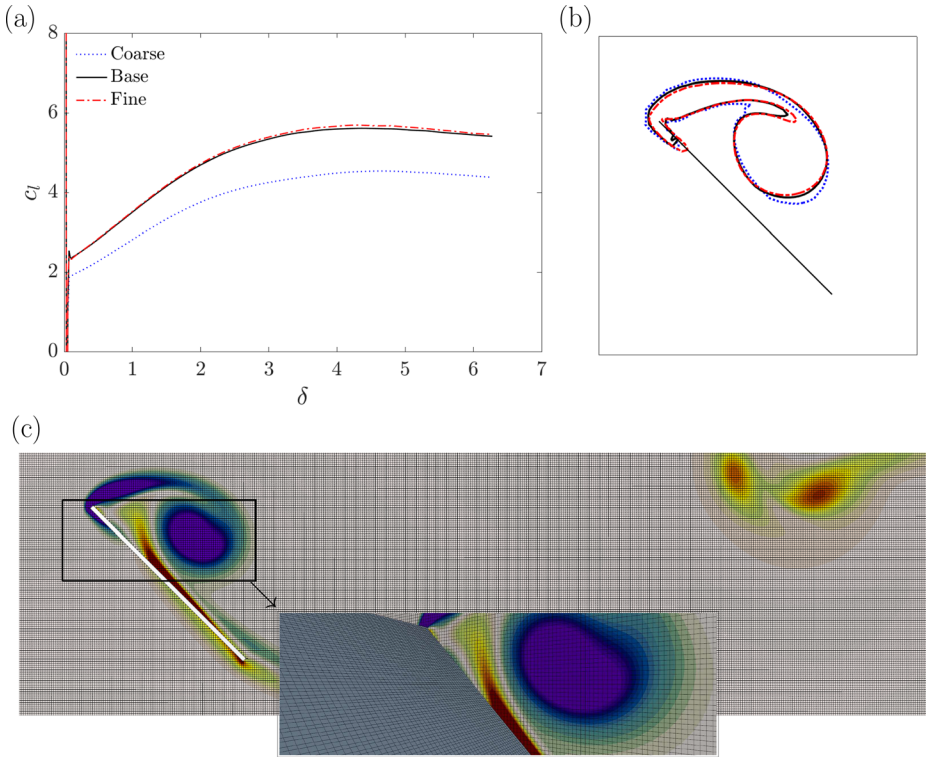

FIG. 3. Influence of grid spacing on (a) sectional lift coefficient and (b) vorticity isolines obtained at $r/c = 2$ in case A. The homogeneous hexahedral mesh in the vicinity and wake of the wing and spanwise vorticity contours are depicted in (c).

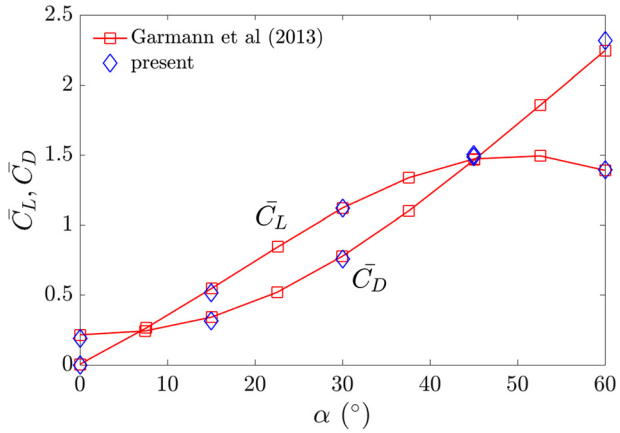

FIG. 4. Time-averaged lift and drag coefficients obtained for an aspect ratio 1, revolving wing using the present approach and reported in Ref. 17.

one, revolving wing. The Reynolds number based on the wing chord and wing speed at midspan is 500, i.e., comparable to that used in the present paper. Spatial and temporal resolutions are similar to those used thereafter ($2\pi/720$ rotation per time step and $\Delta x = 0.02c$). Results are shown in terms of (global) time-averaged lift and drag coefficients in Fig. 4. Very good agreement is observed between both datasets.

V. VORTICITY TRANSPORT FRAMEWORK

The sources and sinks of vorticity contributing to the growth of the LEV system on the wing were quantified using a vorticity transport analysis within a planar control region adjacent to the suction surface of the wing, as shown in Fig. 5. The coordinate system fixed to the wing (which is non-inertial in the rotating cases) is illustrated in Fig. 5, where the x axis is in the chordwise direction, the y axis is normal to the wing, and the z axis is positive inboard for the rotating cases and as shown in Fig. 1 for the translating cases.

The present paper utilizes and advances the transport framework derived by Panah *et al.*[28] and extended to a non-inertial, rotating

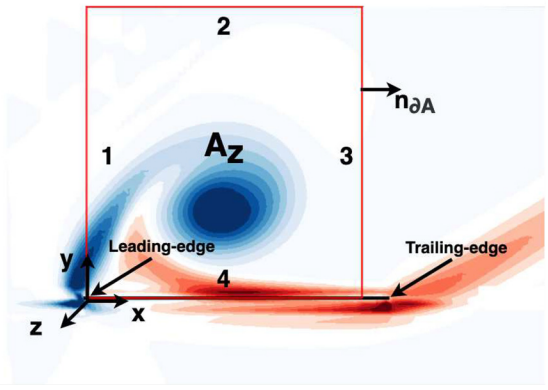

FIG. 5. The planar control region (red box) in which the vorticity transport analysis is conducted.

reference frame by Wabick *et al.*[34] The rate of change of circulation, with constant-reference-frame angular velocity $\boldsymbol{\Omega} = (\Omega_x, \Omega_y, \Omega_z)$, is given by

$$\begin{aligned}\frac{d\Gamma}{dt} = &-\oint_{\partial A_z} (\mathbf{u}\cdot\boldsymbol{n}_{\partial A})\omega_z\, ds - \int_{A_z}\left(u_z\frac{\partial \omega_z}{\partial z}\right) dA \\ &+\int_{A_z}\left(\omega_x\frac{\partial u_z}{\partial x}+\omega_y\frac{\partial u_z}{\partial y}\right) dA + \frac{1}{\rho}\int_{\text{bound 4}}\left(\frac{\partial p}{\partial x}+\Omega_y^2 x\right) dx \\ &-\oint_{\partial A_z} (\mathbf{u}\cdot\mathbf{n}_{\partial A})2\Omega_z\, ds + \int_{A_z} 2\left(\Omega_x\frac{\partial u_z}{\partial x}+\Omega_y\frac{\partial u_z}{\partial y}\right) dA. \end{aligned} \tag{3}$$

The velocity and vorticity values presented in Eq. (3) are represented in the non-inertial frame fixed to the wing. The first term on the right-hand side of Eq. (3) describes the in-plane convection across the control region boundaries (IPCF). This includes the shear-layer flux which is the primary source of LEV circulation. If the LEV is stable, there is negligible in-plane convective flux of circulation across boundaries 2 and 3, such that the shear-layer contribution dominates the IPCF. The second term describes the contribution due to the spanwise convective flux (SPCF), or transport due to the convection of vorticity in the direction normal to the plane of the control region. The third term describes the contribution due to the tilting of free vorticity captured within the non-inertial reference frame. Although vorticity tilting cannot affect the strength of a vortex tube surrounded by inviscid fluid, it can make a finite net contribution here due to the continuous distribution of vorticity and finite extent of the control region. The fourth term, which is only evaluated on boundary 4 (the surface of the wing), approximates the diffusive flux of vorticity from the surface. Diffusive and turbulent transport are neglected in this analysis, except on the surface of the wing (boundary 4), where diffusive transport dominates.

The third line of Eq. (3) contains terms related to Coriolis accelerations ($-2\boldsymbol{\Omega}\times\mathbf{u}$) in the non-inertial reference frame attached to the revolving wing. The fifth term is identically zero for the cases examined in this study, since $\Omega_z = 0$. However, it has the same form as the IPCF and, therefore, can be interpreted as a correction to the IPCF measured within the non-inertial reference frame due to the apparent solid-body rotation introduced by a rotation of the reference frame about an axis normal to the control region. The final term is the Coriolis tilting term. The physical and Coriolis tilting terms will be further analyzed and interpreted in Sec. VI D.

Prior to computing the terms of Eq. (3), the computed pressure distribution and velocity vectors in chordwise planes were linearly interpolated onto a Cartesian grid rotated 45° such that the grid was aligned with the wing chord. The interpolation was conducted separately above and below the wing in order to prevent interpolation across the solid body. The resulting data sets were smoothed using a $3\times3\times3$ box filter, except for points on the wing surface, before joining the top and bottom portions. Derivatives were computed numerically using second-order centered finite differences, and integrals were computed using rectangular integration. The final resolution of the grid was $0.02c$ in the x and y directions and $0.1c$ in the z direction.

Other studies employ either a rectangular control region of smaller chordwise extent, such as to contain only the LEV system,[28,32,34] or a control region with boundaries that conform to the vortex.[5,26,27] In the present work, a rectangular control region was

selected to capture the diffusive flux of vorticity generated on the suction surface of the wing, and its size results from a compromise between exclusion of the trailing-edge vortex (TEV) and maximum inclusion of the LEV (which is unstable in some cases). Since our objective is to characterize the sources of circulation governing the strength of the LEV system, the upstream boundary is placed at the leading-edge, capturing the transport of vorticity into the structure via the shear layer. A small region of the shear layer is not captured within the control region; its circulation is typically approximately 20% of that inside the control region when the LEV resides within the control region, for the cases examined in this study. Boundaries 2 and 3 are placed to mitigate interaction with the TEV while still containing the stable LEV structure, with Boundary 2 lying one chord above the wing surface and Boundary 3 lying 0.9 chords from the leading edge. Since this study focuses on LEV stability, control region boundaries are placed to be most meaningful when the LEV is stably attached. While the definition of the control region does not affect the validity of Eq. (3), it can have some effect on the magnitudes of the terms, and these effects are discussed in Sec. VI C.

VI. RESULTS

A. Flow structure

In this section, we examine the effects of independently including or excluding inflow velocity gradient and rotational accelerations on the global flow structure, the evolution of the vorticity field in a chordwise plane near the wing root, and spanwise flow over the suction surface of the wing. Specifically, their influences on global flow patterns, distribution of spanwise vorticity, lift force, and vorticity transport mechanisms are discussed.

1. Global flow patterns

Figure 6 (Multimedia view) contains three-dimensional volume renderings of dimensionless vorticity magnitude $\omega^* = \omega c/u_{\theta,(r/c=2)}$ [where ω is the vorticity magnitude, $u_\theta(r)$ is the azimuthal inflow velocity, and r is the distance from the center of the domain and wing rotation axis], for each of cases A–D. In the translational cases, the same velocity scale is used as for the rotational cases. A comparison of the four cases in Fig. 6 demonstrates that inflow velocity profile and rotational accelerations individually have a significant impact on flow structure at different times during the wing rotation.

At $\delta = 0.349$, the leading-edge, trailing-edge, and tip vortices are visible on the wing for all four cases, but the effects of velocity gradient are already apparent as spanwise variability in the sizes of the LEVs and TEVs is clearly evident. By $\delta = 1.05$, a striking disparity between the variable inflow and uniform inflow cases has developed, such that the chordwise convection of the LEV and TEV structures varies significantly over the span of the wing, and the LEV is beginning to form an arch structure over the outboard region of the wing for cases A and B. The flow is much more uniform along the span for cases C and D. Importantly, the differences in the rendered vorticity fields between cases A and B, and between cases C and D, are very minimal, suggesting that rotational accelerations have little influence on the early evolution of the flow.

By $\delta = 2.09$, conical LEV structures are clearly evident for cases A and B, further demonstrating dominance of the inflow velocity profile on the early development of the LEV. Over the outboard region of the wing, multiple LEV structures have formed and shed, resulting in apparent bifurcations of the LEV structure around the 30% spanwise position. Similar shedding occurs for cases C and D, but the evolution is more uniform over the span of the wing.

At $\delta = 3.14$, the attached conical LEV is evident over the inboard third of the wing for case A. Outboard of that region, shed vortices are nearly perpendicular to the leading edge. The inboard LEV behavior is consistent with other observations in the literature for regions sufficiently close to the axis of rotation.[16,37,38] Case B, which lacks the rotational accelerations, exhibits similar stability although the inboard LEV has become larger, distinguishing the two cases. This suggests that rotational accelerations become important later in the maneuver. Jardin and David[7] also found that an LEV formed in the presence of rotational accelerations and inflow velocity gradient was more compact than one formed with only the inflow velocity gradient and suggested that the velocity gradient is a key contributor to maintaining a strong, attached LEV for shorter stroke lengths. Periodic shedding of the LEV and TEV system is apparent in both cases C and D. By $\delta = 4.19$, instabilities have grown on the LEV structures, which somewhat obscures the large-scale topology; however, cases A and B are clearly distinct from C and D, maintaining compact, attached, conical LEVs in the inboard region of the wing. Figure 6 (Multimedia view) demonstrates periodic shedding of the LEV in case D.

2. Spanwise vorticity distributions

The visualizations of the 3D vortex structures discussed in Sec. VI A 1 indicate that rotational accelerations are most active later in the rotation, while inflow velocity gradients are important throughout the rotation. The differences between the cases are greatest for the inboard regions of the rotating wings, where the effects of the inflow velocity gradient and rotational accelerations are strongest. Figure 7 (Multimedia view) shows the evolution of the vorticity fields in the chordwise planes at $r/c = 2$ for the rotating wings and, correspondingly, 1.5 chords inboard from the root of the translating wing. For simplicity, we will subsequently refer to this position as $r/c = 2$ for both rotating and translating wings. Consistent with the 3D flow structure renderings, at $\delta = 0.175$, the spanwise vorticity fields appear nearly identical for all four cases; however, by $\delta = 1.05$, notable differences are apparent. In particular, the cases without inflow velocity gradients (C and D) have significantly lower values of vorticity in the LEV, further illuminating the impact of inflow profile on the early development of the LEV. It is noteworthy that the vorticity fields in cases A and B and cases C and D are nearly identical at this stage, indicating that rotational effects are not yet manifest on the LEV structure.

As the wing stroke progresses, the behaviors of the four cases diverge. By $\delta = 3.14$, the vortex has moved further away from the wing in case B than in case A; however, additional simulations of case B, extending to $\delta = 17$ (not shown), revealed that the LEV remained stable. In contrast, for case C, the LEV convects away from the wing early in the rotation at $r/c = 2$, but the attachment of the vortex is restored late in the rotation (i.e., $\delta = 4.19$), though with significantly lower peak vorticity than cases A and B, providing further evidence that rotational accelerations assist LEV stability later in the motion. Case D sheds leading- and trailing-edge vortices in an alternating manner as can be seen in Fig. 7 (Multimedia view). Figure 7 (Multimedia view) also reveals a slight oscillation in the LEV position in case B which is not present in case A. Thus, the inflow velocity gradient appears to strengthen the LEV while assisting attachment, while

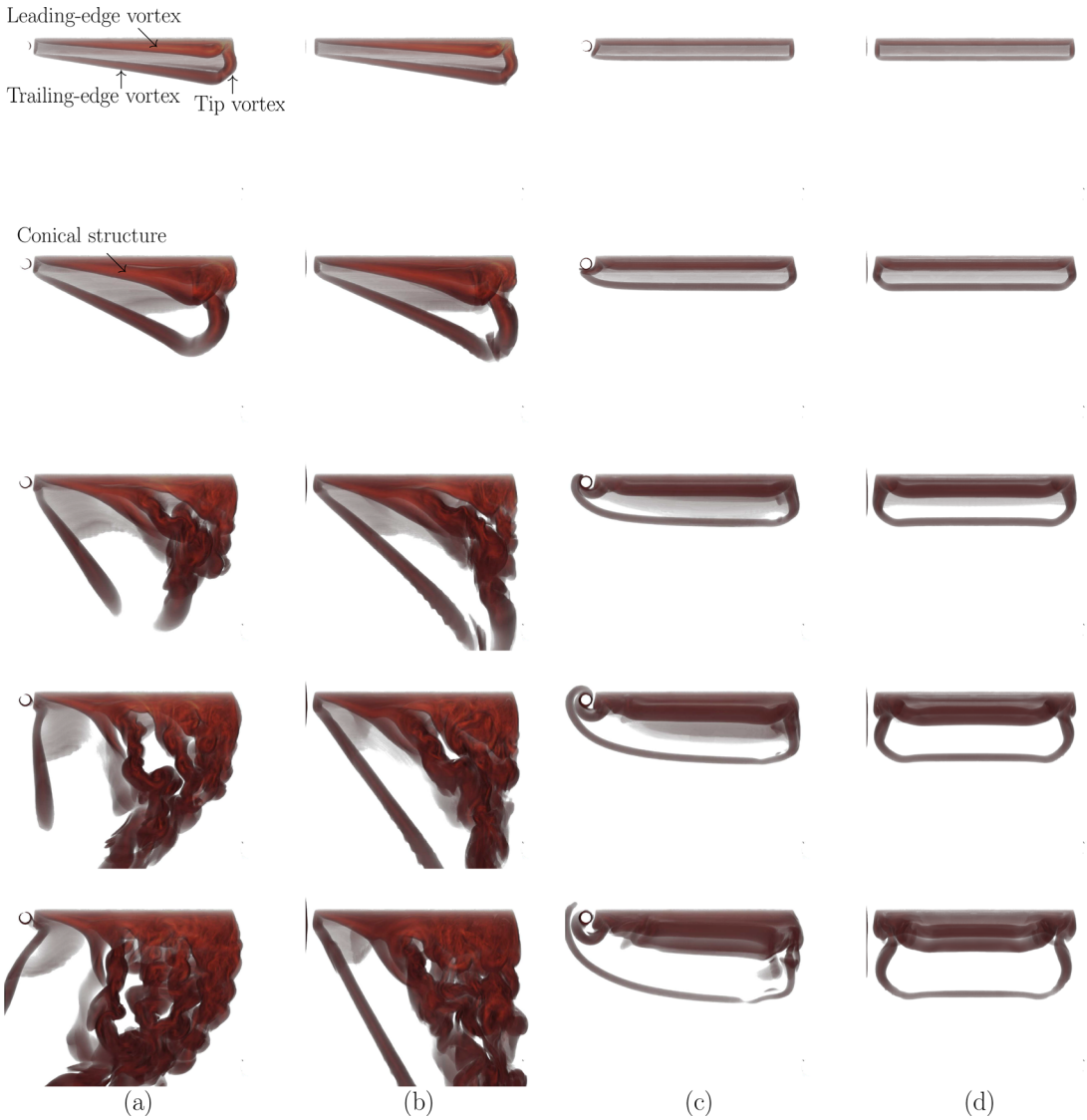

FIG. 6. Three-dimensional volume renderings of dimensionless vorticity magnitude. (a) Case A, (b) case B, (c) case C, and (d) case D at $\delta = (0.349, 1.05, 2.09, 3.14, 4.19)$ from top to bottom, respectively. Note that the plotted vorticity range is $(3 \leq \omega c/u_{\theta,(r/c=2)} \leq 300)$; however, values greater than approximately 130 are interior to the vortex structure and masked by the lower values on the exterior. The visible range is approximately 3 (dark red) to 130 (light red) and opacity increases with vorticity strength. Multimedia available online.

rotational accelerations work to maintain LEV proximity to the wing surface.

3. Spanwise velocity fields

Figure 8 (Multimedia view) contains isocontours of spanwise velocity in the vicinity of the wing, to help elucidate the effects of inflow velocity gradient and rotational accelerations on spanwise transport over the wing surface. The leading-edge vortex and shear-layer loci are indicated using an isocontour of $\omega_z = -200$ (s^{-1}). Since the flow within the simulation domain is circumferential in cases A and C, the isocontours reveal a weak, diagonal gradient in spanwise flow within the plane due to the 45° pitch angle of the wing. Outboard flow is clearly evident over the suction surface of the wing for cases A–C, but is notably absent for case D. This is similar to flow behavior seen in Ref. 7 where outboard flow was shown to be negligible when neither aspect of rotational motion is active. Rotational accelerations were also shown by Jardin to substantially alter outboard flow.[18]

A comparison of Figs. 7 and 8 shows that the tendency for the LEV to remain attached is concomitant with the presence of outboard spanwise flow as noted in prior studies.[12,16,39] Outboard spanwise flow is present throughout the rotation of cases A and B (which have inflow velocity gradients) and late in the rotation for case C (which has only rotational accelerations). In cases A and B, the outboard flow is

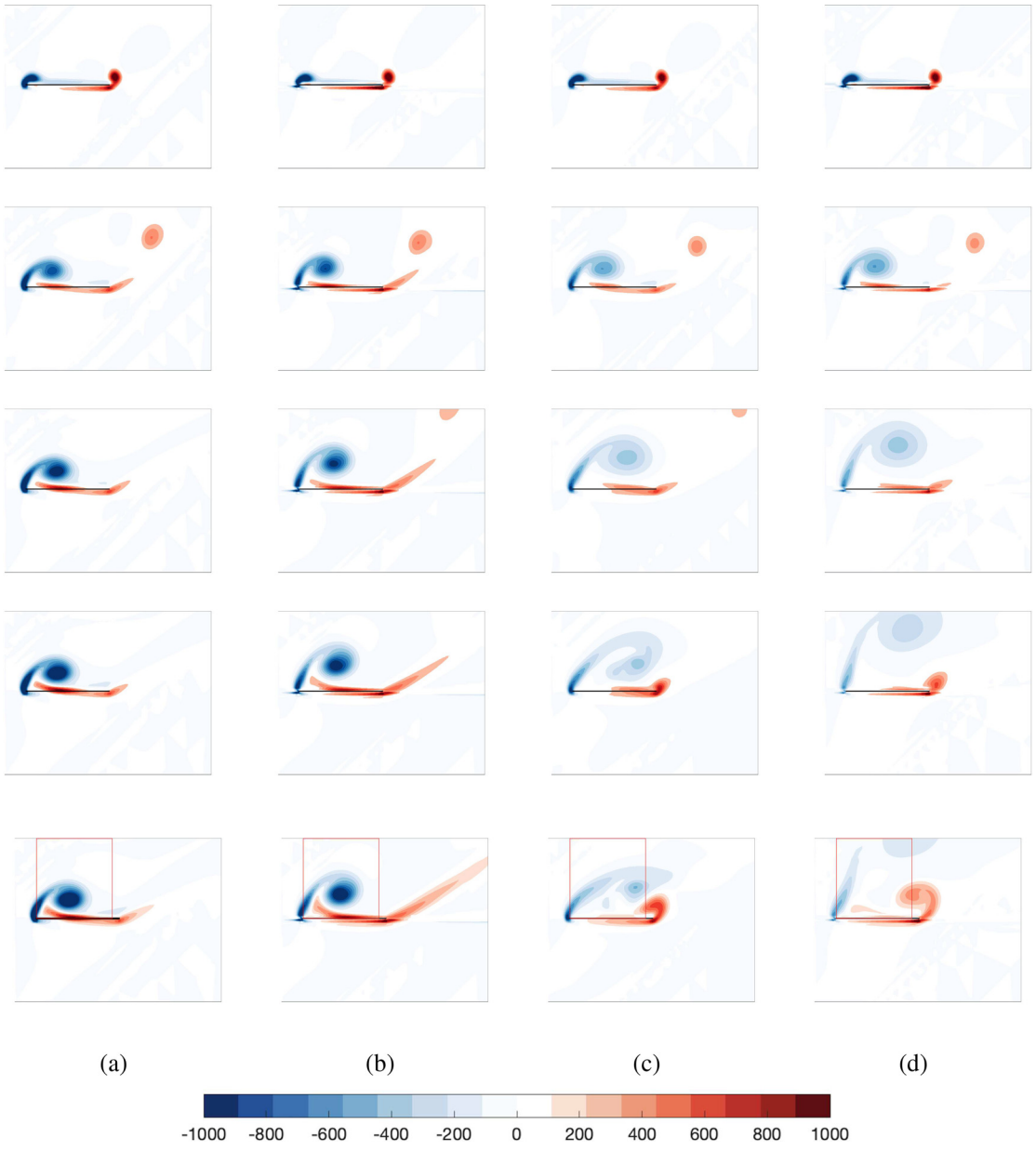

FIG. 7. Spanwise vorticity contour plots (1/s) at $r/c = 2$ for (a) case A, (b) case B, (c) case C, and (d) case D at $\delta = (0.175, 1.05, 2.09, 3.14, 4.19)$ from top to bottom, respectively. Multimedia available online.

significantly stronger than in case C, and the high-velocity regions are aligned with the vortex cores. This indicates that the inflow velocity gradient is a much stronger driver of spanwise flow than rotational accelerations.

While many studies have noted the concurrence of LEV stability and spanwise flow, there are varying views on the dominating mechanisms by which spanwise flow assists attachment. For example, Maxworthy[11] and Ellington *et al.*[12] argued that the presence of spanwise flow acts as an outboard sink of vorticity, while Lentink and Dickinson[16] argued that spanwise flow alters rotational accelerations to stabilize the LEV. Chen *et al.*[40] developed closed-form expressions for the circulation and position of the LEV on a rotating wing by employing the Brown–Michael vortex[41] combined with a Lagrangian spanwise transport model and found good agreement with simulations at $Re = O(100)$ and experiments at $Re = O(1000)$. In Sec. VI C, we examine the extent to which spanwise transport of vorticity governs vortex strength in comparison with other mechanisms of vorticity transport.

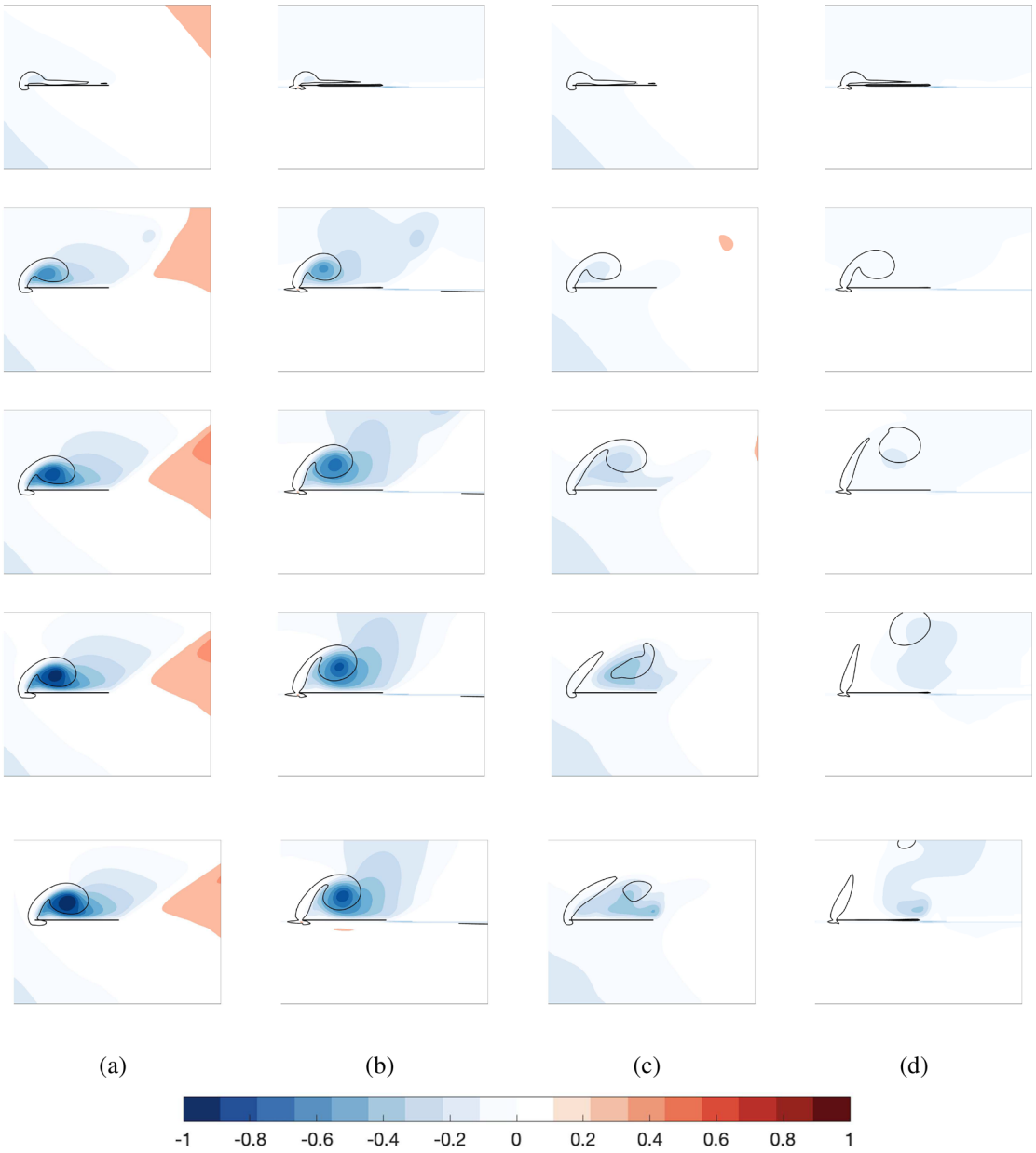

FIG. 8. Spanwise velocity contour plots (m/s) with spanwise vorticity isolines [$\omega_z = -200$ (s^{-1})] of (a) case A, (b) case B, (c) case C, and (d) case D at $\delta = (0.175, 1.05, 2.09, 3.14, 4.19)$ from top to bottom, respectively. Note that positive spanwise velocity is oriented in the inboard direction in the local reference frame defined in Fig. 5. Multimedia available online.

B. Lift coefficients

Sectional lift coefficients at $r/c = 2$ are shown in Fig. 9. The sectional lift coefficient is defined as $c_l = \frac{2dL}{(\rho c u^2)}$, where dL is the sectional lift at $r/c = 2$, c is the chord length, ρ is the fluid density, and u is the inflow velocity at $r/c = 2$. Specifically, dL is obtained by integrating pressure and viscous forces experienced by the wing in a spanwise strip of width $0.01R$, projecting the resulting force on the global vertical axis and dividing it by $0.01R$ such that dL has dimensions N/m. The lift generated in case A is substantially larger than that of the other cases and is concomitant with a compact LEV that resides close to the wing surface, as shown in Sec. VI A 2. In contrast, case D exhibits the lowest lift force through most of the maneuver and appears to evince the early stage of the periodic vortex shedding pattern suggested by Fig. 7 in which there is a corresponding oscillation of the lift. A slight oscillation in the lift of case B is concomitant with the LEV oscillatory behavior noted in Sec. VI A 2.

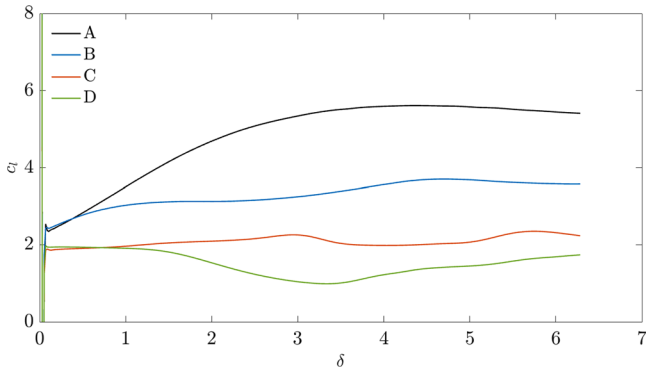

FIG. 9. Sectional lift coefficients at $r/c = 2.0$ for cases A–D.

Each case displays an inertial peak in sectional lift coefficient due to the impulsive start before settling to an initial circulatory lift magnitude. Remarkably, this initial lift appears to be dominated, almost exclusively, by whether or not an inflow velocity gradient is present and is substantially unaffected by rotational accelerations. The influence of the rotational accelerations becomes evident within the first chord length of motion, where the cases without rotational accelerations (B and D) begin to deviate from cases A and C, respectively. The deviations reach maxima by approximately three chord lengths of travel.

As may be anticipated, the sectional lift curves appear to strongly correlate with the behavior of the LEVs as shown in Fig. 7. The difference in lift between cases A and B can be attributed to the movement of the vortex away from the wing surface in case B. On the other hand, the weaker lift in cases C and D can be attributed primarily to the much weaker vortex structures, and the difference between the lift of cases C and D is due to the shedding of the vortex in case D. Thus, the lift appears to be directly governed by the impact of the inflow velocity profile on LEV strength and the influence of the rotational accelerations on its proximity to the wing surface.

C. Vorticity transport

Figure 10 displays the evolution of the terms of Eq. (3) for cases A–D within the planar control region shown in Fig. 5. To verify closure, the values of the left- and right-hand sides of Eq. (3) are also plotted. The differences are primarily due to truncation errors in the numerical evaluation of the terms in Eq. (3). In most cases, the discrepancy is small compared to the magnitudes of the terms dominating the circulation budget; however, there are significant disparities early in the motion, where the quantities change rapidly.

Viewing case A as the benchmark for comparison with the other cases, several distinct characteristics are apparent. The IPCF is the primary source of LEV circulation. As will be shown later, it is dominated by the shear-layer contribution. It is also negatively correlated with the diffusive flux, as noted in earlier studies,[28,31] since the two fluxes are coupled by the suction peak near the leading edge, which affects both the leading-edge shear-layer strength as well as the subsequent pressure recovery that determines the magnitude of the surface diffusive flux. Interestingly, the diffusive flux is larger than other sinks of circulation throughout the maneuver. Spanwise convection, tilting, and Coriolis tilting act primarily as sinks throughout the motion, although the tilting and spanwise convective flux make negative (i.e., strengthening) contributions early and late in the motion, respectively. This oscillatory behavior exists despite that the outboard spanwise velocity increases monotonically in magnitude and spatial extent, throughout the motion, as illustrated in Fig. 8(a). Similar to the IPCF and surface-diffusive fluxes, the SPCF and tilting fluxes also exhibit a high degree of symmetry. The reason for this behavior will be discussed in Sec. VI D.

Removal of the rotational accelerations from case A results in some striking differences in the magnitudes of the transport fluxes, which are apparent when comparing cases A and B in Figs. 10(a) and 10(b), respectively. Importantly, the IPCF is significantly weaker in case B than in case A, and the corresponding diffusive flux is also reduced. However, this effect is not a robust effect of rotational accelerations, as corresponding differences are not evident between cases C and D. Figure 11 isolates the shear-layer contributions to the IPCF (i.e., that through boundary 1 of the control region) for each of the four cases. Comparing Fig. 11 with Figs. 10(a) and 10(b), it is evident that the IPCF is essentially equal to the shear-layer contribution since there are negligible fluxes of circulation across boundaries 2 and 3 of the control region in cases A and B. The reduction in the shear-layer contribution in case B is due to a weaker suction peak near the leading edge, which is likely caused by the LEV residing further from the leading-edge, as discussed in Sec. VI A 2. Significant correlation between the SPCF and tilting fluxes also persists in case B; however, crossover of the two fluxes is delayed until approximately $\delta = 6$. This may be caused by the slower growth of the LEV, due to the weaker shear-layer flux.

In cases C and D, the LEV system is more volatile such that its trajectory results in significant fluxes of vorticity across boundaries 2 and 3 at certain times during the motion, making the values of the terms in Eq. (3) sensitive to the placement of boundaries 2 and 3 of the control region. For cases C and D, vortex interaction with the downstream control-region boundary occurs at approximately $\delta = 1.5$, as can be discerned by comparing the evolution of the shear-layer contributions in Fig. 11 with the IPCF values plotted in Figs. 10(c) and 10(d). It should be noted that, beyond this time, the circulation budget is still closed and Eq. (3) is still valid within the control region; however, it does not capture the entire vortex system. Nevertheless, the shear-layer contributions provided in Fig. 11 are accurately quantified throughout the motion.

In contrast to cases A and B, the shear-layer contributions for cases C and D exhibit an initial decline in magnitude, reaching a local minimum at approximately $\delta = 2$ in case C and $\delta = 3.2$ in case D. The diffusive flux correspondingly drops in magnitude as the LEV moves away from the wing surface. In case C, the shear-layer contribution subsequently recovers, reaching a local maximum at approximately $\delta = 3$, and sustaining a relatively constant value during the remainder of the motion. The recovery is commensurate with the descent of the LEV core toward the surface, as shown in Fig. 7(c). Case D exhibits a similar, but weaker, recovery at approximately $\delta = 5.7$, corresponding to the formation of a second LEV after the first vortex sheds, as illustrated in Fig. 7(d) (Multimedia view). Prior to the advection of LEV vorticity out of the control region, the tilting, Coriolis tilting, and SPCF contributions remain small in comparison with the IPCF (shear-layer) and diffusive fluxes. Later in the motion, despite that the complete LEV system is not captured within the control region, the symmetries between the IPCF and diffusive fluxes, and between the SPCF and tilting fluxes, remain remarkably strong for cases C and D.

In summary, the systematic removal of the inflow velocity gradient and/or the rotational accelerations from the full rotating case (case

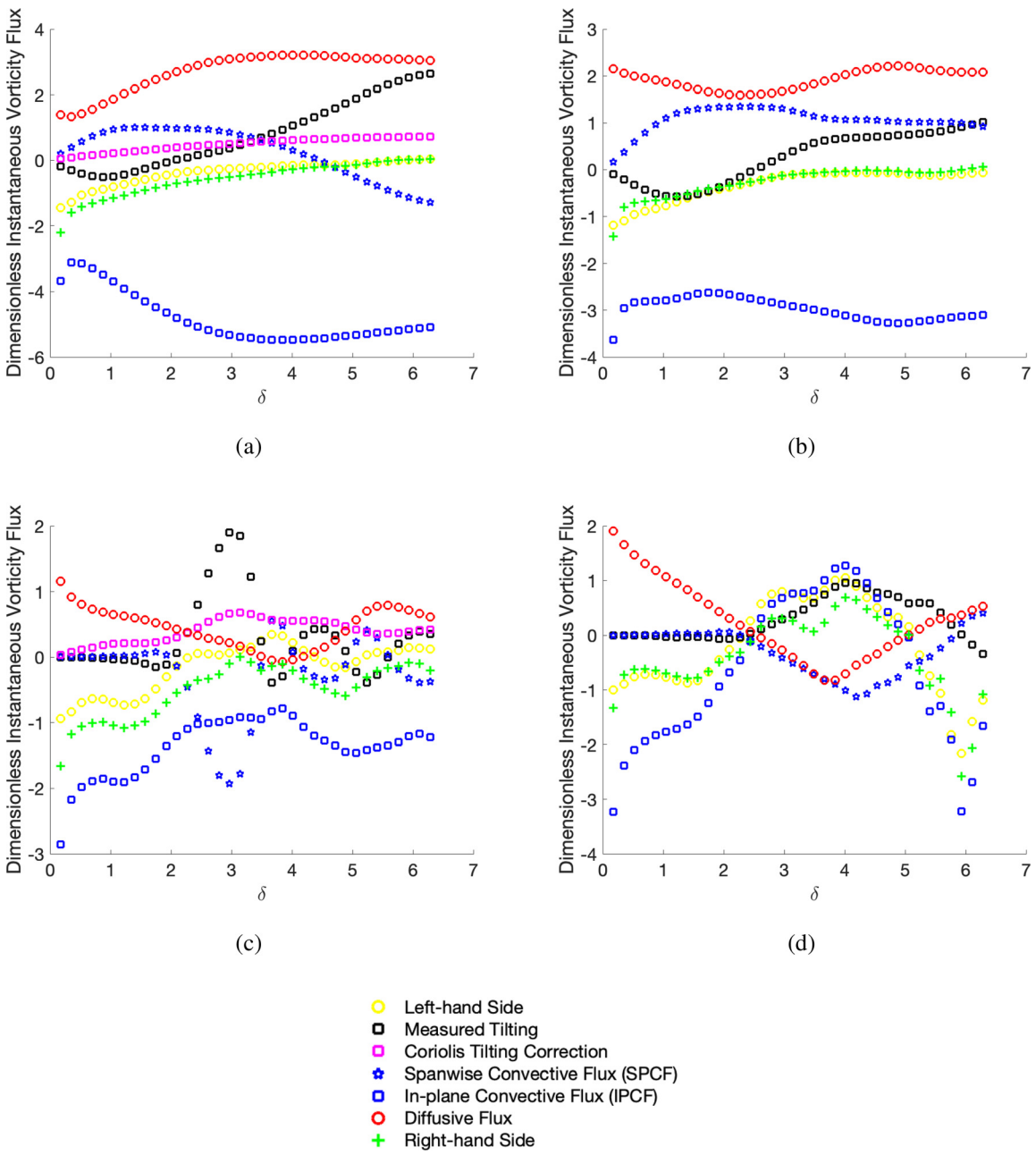

FIG. 10. Dimensionless vorticity transport budget of (a) case A, (b) case B, (c) case C, and (d) case D. $\frac{d\Gamma^*}{dt} = \frac{d\Gamma}{dt} * (\frac{1}{r\Omega})^2$, where $r\Omega$ is constant across all 4 cases at r/c = 2.0.

A) results in substantial reductions in the typical magnitudes of the shear-layer flux. It is also evident in comparing cases A and B (where there are not strong convective vorticity fluxes across the downstream boundary) that the removal of the rotational accelerations also diminishes the diffusive flux. The contrary behaviors of the SPCF and tilting flux are also robust in all cases; the removal of the inflow velocity gradient in cases C and D results in a substantial decline in their contributions early in the motion.

Inspection of the Coriolis tilting contributions in cases A and C reveals that, in both cases, the term is positive, or opposite in sign to the LEV, as previously noted by Eldredge and Jones[5] and Werner *et al.*[33] (see also more recent work by Chen *et al.*[42]). Although the contribution of the Coriolis term in case C is significant in comparison with the other terms, and relatively insignificant in case A, the magnitudes of the Coriolis contributions are similar between the two cases. Considering the minimal contribution of Coriolis tilting to the total

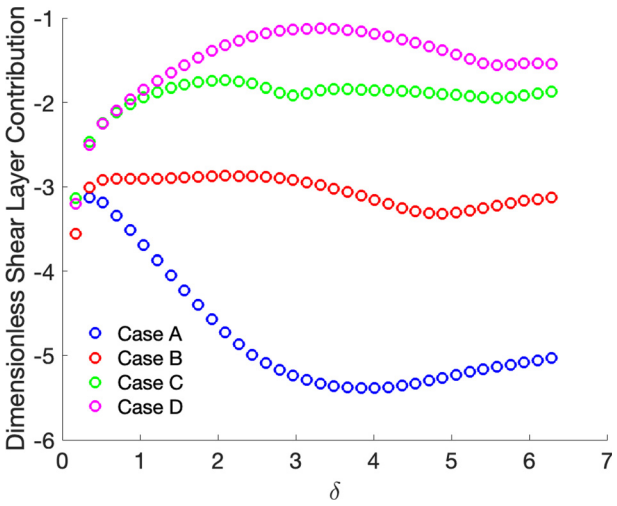

FIG. 11. The non-dimensional shear-layer flux contributions $\left(\frac{d\Gamma^*}{dt}\right)$ of all four cases (in-plane flux across boundary 1).

circulation budget in case A, and the similar observation by Wabick *et al.*[34] at $Re_C = 10^4$, it appears that the Coriolis tilting term is not a robust regulator of LEV strength on revolving wings.

D. Interpretation of spanwise convective and tilting transport terms

To understand the source of the negative correlation between the tilting flux and spanwise convective flux, we first consider the spanwise convective term. As shown in Appendix A, the SPCF can be expressed as

$$-\int_{A_z}\left(u_z\frac{\partial\omega_z}{\partial z}\right)dA = -\oint_{\partial A_z} u_z\frac{\partial}{\partial z}(\mathbf{u}\cdot\,\mathrm{d}\mathbf{s}) - \int_{A_z}\left(\omega_x\frac{\partial u_z}{\partial x}+\omega_y\frac{\partial u_z}{\partial y}\right)\mathrm{d}A. \quad (4)$$

The first term on the right-hand side of Eq. (4) can be physically interpreted as out-of-plane transport due to a gradient in circulation. The term captures the essence of the contribution to circulation associated with spanwise convection. This new term will be hereafter referred to as the out-of-plane circulation flux (OPCF). The second term on the right-hand side of Eq. (4) is the negative of the tilting term in Eq. (3). This result provides insight into the correlation between the SPCF and tilting fluxes observed in Fig. 10, as well as the action of the tilting flux. That the tilting flux is a constituent of the spanwise convective flux is a consequence of the solenoidal condition, which requires that the vorticity field be three-dimensional if there is a nonzero contribution to the circulation by out-of-plane convection. Therefore, tilting appears to be inevitable if a spanwise convective flux contributes to the circulation budget.

By substituting Eq. (4) into Eq. (3), we replace both the SPCF and tilting terms with the OPCF. As shown in Appendix B, the Coriolis tilting flux can also be expressed as a contour integral in terms of the apparent velocity field induced by the solid-body-rotation of the non-inertial reference frame ($\mathbf{u}' = \boldsymbol{\Omega}\times\mathbf{r}$). Equation (3) can, therefore, be written as

$$\frac{d\Gamma}{dt} = -\oint_{\partial A_z}(\mathbf{u}\cdot\boldsymbol{n}_{\partial A})\omega_z\,\mathrm{d}s - \oint_{\partial A_z} u_z\frac{\partial}{\partial z}(\mathbf{u}\cdot\mathrm{d}\boldsymbol{s}) + \frac{1}{\rho}\int_{\text{bound 4}}\left(\frac{\partial p}{\partial x}+\Omega_y^2 x\right)dx - \oint_{\partial A_z}(\mathbf{u}\cdot\mathbf{n}_{\partial A})2\Omega_z\,ds - 2\oint_{\partial A_z} u_z\frac{\partial}{\partial z}(\mathbf{u}'\cdot\,\mathrm{d}\mathbf{s}), \quad (5)$$

where the last term is the Coriolis tilting term. It is evident that the Coriolis terms on the second line of Eq. (5) have the identical forms as the IPCF and OPCF and can be combined with those terms to produce a new form of the integral vorticity transport equation

$$\frac{d\Gamma}{dt} = -\oint_{\partial A_z} u_z\frac{\partial}{\partial z}\left((\mathbf{u}+2\mathbf{u}')\cdot\,\mathrm{d}\mathbf{s}\right) - \oint_{\partial A_z}(\mathbf{u}\cdot\boldsymbol{n}_{\partial A})(\omega_z+2\Omega_z)\,ds + \frac{1}{\rho}\int_{\text{bound 4}}\frac{\partial p}{\partial x}+\Omega_y^2 x\,dx. \quad (6)$$

The first term on the right-hand side of Eq. (6) represents three-dimensional convective transport, including Coriolis tilting. With the inclusion of Coriolis tilting, we will refer to this term as $\text{OPCF}_{\text{Cor.}}$ As noted above, spanwise convection (as quantified in the replaced SPCF term) and vorticity tilting are an integrated phenomenon, and therefore, it is appropriate to consider their net effect within the circulation budget. The physical interpretation of Coriolis tilting in the context of this budget will be discussed below. The high degree of symmetry exhibited between the tilting and spanwise convective fluxes in Fig. 10 demonstrates that the actual physical out-of-plane convection of vorticity, represented by the OPCF_{Cor} term, contributes significantly less to the overall circulation budget than the spanwise convective flux. This contribution will be quantified in Sec. VI E.

The second term in Eq. (6) is the in-plane convective transport term (IPCF), which includes the in-plane Coriolis contribution. This new term will be referred to as $\text{IPCF}_{\text{Cor.}}$ It should be noted that, in the present case, $\Omega_z = 0$, and therefore, there is no in-plane Coriolis contribution for the maneuvers included in this study. The third term is the diffusive flux from the wing surface, and it retains the same form as in Eq. (3).

Although the analysis presented in Sec. VI C demonstrated Coriolis tilting to be a small contributor to the circulation budget, and overwhelmed by the contribution to the shear-layer flux attributed to the rotational accelerations, a physical interpretation of the Coriolis tilting flux is still fundamentally useful. Vorticity in the non-inertial frame is augmented by the *planetary* vorticity, as designated by Werner *et al.*,[33] in analogy with vorticity acquired due to the spin of a planet. They described Coriolis tilting as the tilting of planetary vorticity within the rotating coordinate system by a vertical gradient of Coriolis acceleration caused by a vertical gradient in spanwise flow. In the present work, we adopt a literal interpretation of the planetary vorticity, defined by the kinematics of the non-inertial reference frame, which is therefore unable to tilt in the same sense as free vorticity. Consequently, we interpret Coriolis tilting as the apparent vanishing of vorticity associated with the tilting of free vorticity that is initially parallel to the rotation axis (which is augmented by the planetary rotation) into the radial direction (which is not augmented by the planetary rotation). The relative quantitative insignificance of the Coriolis tilting term in the present study is due to the fact that the magnitude of the planetary vorticity 2Ω is much smaller than peak vorticity values in the

LEV at the section studied here. It is possible that, in other applications with lower vorticity magnitude, the Coriolis tilting term may constitute a more significant portion of the $OPCF_{Cor.}$ However, we emphasize that Eqs. (4) and (6) demonstrate that SPCF, tilting, and Coriolis tilting contributions to the circulation budget are not independent but, rather, a collective consequence of the existence of out-of-plane flow and a three-dimensional vorticity field.

E. Contributions of in-plane and out-of-plane vorticity fluxes

With the primary contributions to the circulation of the LEV system categorized as in-plane convection ($IPCF_{Cor}$), out-of-plane convection ($OPCF_{Cor}$), and the surface diffusive flux in Eq. (6), we now consider the relative importance of their roles in governing LEV strength. As demonstrated in Sec. VI C, the leading-edge shear-layer flux is the dominant contributor to the IPCF and thereby the growth of the LEV system. The $OPCF_{Cor}$ and diffusive fluxes regulate growth by acting as circulation sinks. We can now clearly illustrate the relative importance of these two terms and the impact of rotational accelerations and inflow velocity profile on their magnitudes.

Figure 12 shows the evolution of the shear-layer component of $IPCF_{Cor}$, the $OPCF_{Cor}$, and diffusive flux, for cases A–D, throughout the maneuver. Considering Fig. 12(a), it is noteworthy that, for case A, the diffusive flux magnitude exceeds that of the $OPCF_{Cor}$ by at least 50% throughout the motion, despite that LEV stability was found to be

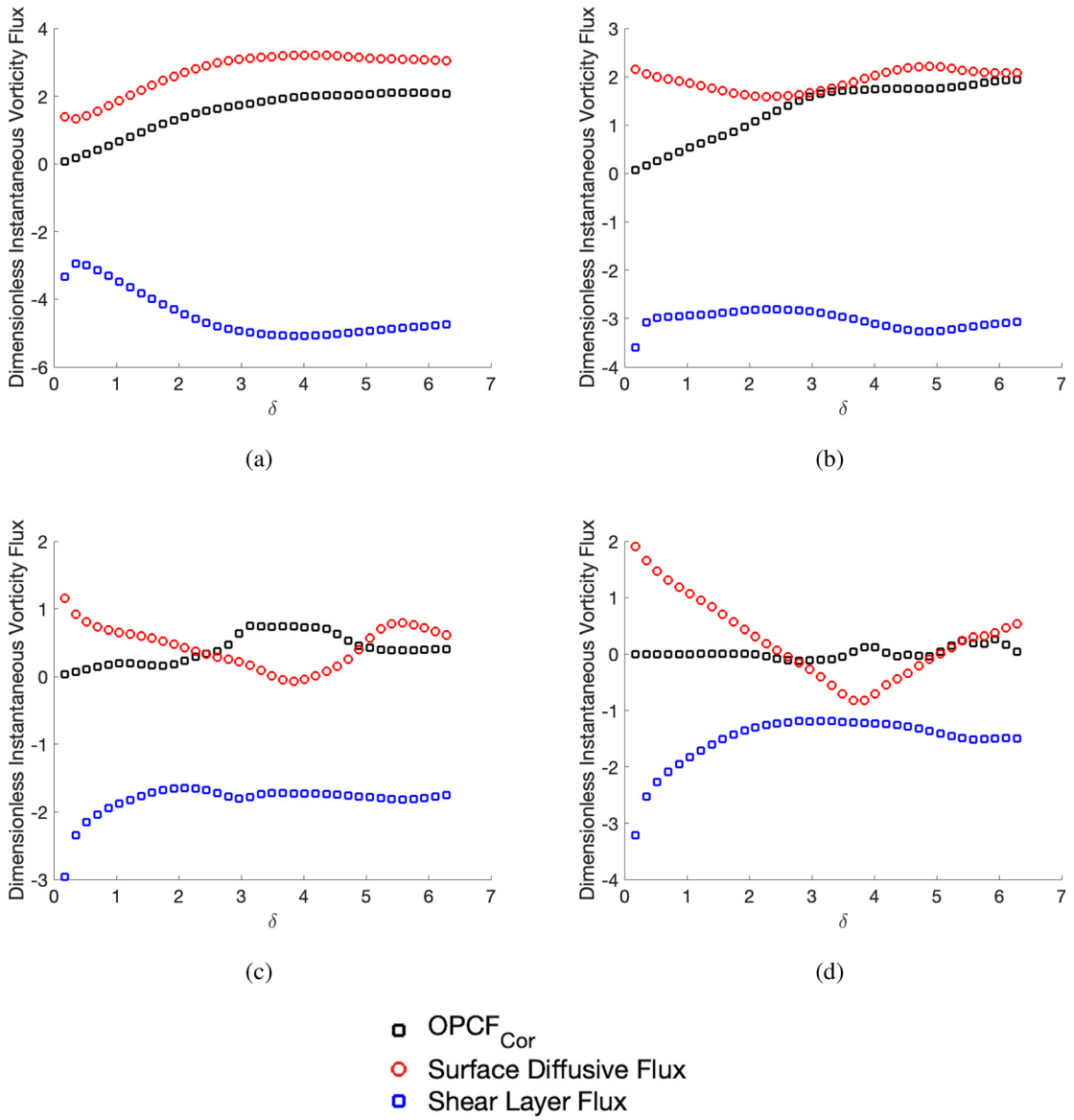

FIG. 12. Relative contributions of $OPCF_{Cor}$, shear-layer flux, and surface-diffusive flux for (a) case A, (b) case B, (c) case C, and (d) case D.

concomitant with the existence of spanwise flow. In fact, since $OPCF_{Cor}$ vanishes at the beginning of the motion for all four cases, the diffusive flux initially dominates in each case. When rotational accelerations are removed in case B, there is only a small decline in the $OPCF_{Cor}$, suggesting that $OPCF_{Cor}$ is insensitive to the presence of the rotational accelerations. However, due to the significant reduction in the diffusive flux, the two contributions become comparable over much of the latter half of the motion.

As noted in Sec. VI C, for cases C and D, the control region analysis is not comprehensive for the LEV system after approximately $\delta = 1.5$; however, it is noteworthy that the trajectories of the $OPCF_{Cor}$ are relatively flat for $\delta < 1.5$ in both cases, and remain significantly lower than their counterparts that incorporate inflow velocity gradients. Thus, despite that prior studies have shown the importance of rotational accelerations to LEV stability, this analysis again shows that they do not significantly influence the $OPCF_{Cor}$ and, therefore, do not make a strong impact on LEV stability by invoking the spanwise draining of vorticity from the vortex. This appears to be the case even considering that it was shown in Sec. VI A 3 that the inclusion of rotational accelerations enhanced spanwise flow later in the motion of the wing. In contrast, the inflow velocity profile appears to have a significant impact on the regulation of vortex strength through out-of-plane transport of vorticity.

Given the importance of the diffusive flux of vorticity on vortex strength regulation, illustrated by Fig. 12, it is noteworthy that the Lagrangian analytical model of Chen *et al.*[40] achieved good prediction of vortex strength and position by considering removal of LEV vorticity from a Brown–Michael vortex only by spanwise convection. Thus, it appears that useful practical predictions of LEV behavior can be achieved in some cases without full consideration of all of the transport mechanisms. However, we postulate that the use of Eq. (6) to characterize the salient transport fluxes can be a useful framework for assessing the state of a developing LEV system and provide metrics to guide the design of lifting surfaces that leverage the benefits of rotating wings.

VII. CONCLUSIONS

The rotational motion of wings and blades is known to be associated with greater LEV stability and higher sectional lift coefficients than equivalent translational motion. By systematically introducing the two salient features of rotational motion—rotational accelerations and inflow shear—when and how each aspect was most influential to the growth of the LEV system was demonstrated.

A vorticity transport budget was applied to each of the four cases studied, providing insight into the sources and sinks of vorticity. A strong, negative correlation was observed between the surface diffusive flux and in-plane convective flux (IPCF), as observed in previous studies. In addition, in the present work, a strong negative correlation was also observed between the spanwise convective (SPCF) and tilting fluxes. In an effort to understand the relationship between SPCF and tilting, we demonstrated that these two transport mechanisms are constituents of a new transport term, which we have called the out-of-plane convective flux (OPCF). The OPCF captures the essence of 3D vorticity transport through the control region and provides a clearer interpretation of the effects of three-dimensionality on vortex growth. Based on this result, we assert that SPCF and tilting are kinematically linked due to the solenoidal condition on the vorticity field.

A new formulation of the vorticity transport equation was proposed, which includes Coriolis contributions to the in-plane convective flux ($IPCF_{Cor}$) and out-of-plane convective flux ($OPCF_{Cor}$). Coriolis tilting was physically interpreted as a loss of apparent circulation as tilting of the vorticity vector converts the scalar component of vorticity that is parallel to the rotation axis—and, thus, augmented by the rotation of the non-inertial frame—into directions perpendicular to the rotation axis, where the augmentation vanishes. Although it was found to have a weakening effect on LEV circulation in agreement with Werner *et al.*[33] and Eldredge and Jones,[5] our analysis within a comprehensive circulation budget demonstrated that the Coriolis tilting is not an important contributor, consistent with the observations of Wabick *et al.*[34]

Given that rotational accelerations are known to stabilize LEVs, we sought to understand whether this rotationally driven stabilization is achieved through spanwise transport of vorticity represented by the $OPCF_{Cor}$ term. It was shown that $OPCF_{Cor}$ is insensitive to the presence or absence of rotational accelerations, but is strongly influenced by the inflow velocity profile. It was also found that the regulating effect of $OPCF_{Cor}$ on LEV strength is significantly smaller in magnitude than the surface diffusive flux throughout the maneuver, and especially in the early phase of the motion. These observations, thus, shed light on how global flow attributes influence vortex growth and, therefore, can provide insight into how to leverage attributes of rotating wings to achieve desirable aerodynamic behavior.

ACKNOWLEDGMENTS

The first author was supported, in part, by a fellowship from the University of Iowa Office of Undergraduate Research.

AUTHOR DECLARATIONS

Conflict of Interest

The authors have no conflicts to disclose.

Author Contributions

James H. Paulson: Formal analysis (equal); Software (equal); Visualization (lead); Writing – original draft (equal); Writing – review & editing (equal). **Thierry Jardin:** Conceptualization (equal); Data curation (equal); Formal analysis (equal); Methodology (equal); Software (equal); Visualization (supporting); Writing – original draft (supporting); Writing – review & editing (equal). **James H. J. Buchholz:** Conceptualization (equal); Data curation (equal); Formal analysis (equal); Methodology (equal); Software (equal); Writing – original draft (equal); Writing – review & editing (equal).

DATA AVAILABILITY

The data that support the findings of this study are available from the corresponding author upon reasonable request.

APPENDIX A: EXPANSION OF THE SPANWISE CONVECTIVE FLUX (SPCF)

Substituting $\frac{\partial \omega_z}{\partial z} = \frac{\partial}{\partial z}\left(\frac{\partial u_y}{\partial x} - \frac{\partial u_x}{\partial y}\right)$ and expressing the resulting area integrals as double integrals in x and y over the rectangular control region yields

$$-\int_{A_z}\left(u_z\frac{\partial\omega_z}{\partial z}\right)dA=-\int_{y_1}^{y_2}\left[\int_{x_1}^{x_2}u_z\frac{\partial}{\partial x}\left(\frac{\partial u_y}{\partial z}\right)\mathrm{d}x\right]\mathrm{d}y+\int_{x_1}^{x_2}\left[\int_{y_1}^{y_2}u_z\frac{\partial}{\partial y}\left(\frac{\partial u_x}{\partial z}\right)\mathrm{d}y\right]\mathrm{d}x. \tag{A1}$$

In Eq. (A1), the expressions in the square brackets can be integrated by parts to produce the following expression:

$$-\int_{A_z}\left(u_z\frac{\partial\omega_z}{\partial z}\right)dA=-\int_{y_1}^{y_2}\left[u_z\frac{\partial u_y}{\partial z}\right]_{x_1}^{x_2}\mathrm{d}y+\int_{x_1}^{x_2}\left[u_z\frac{\partial u_x}{\partial z}\right]_{y_1}^{y_2}\mathrm{d}x+\int_{x_1}^{x_2}\int_{y_1}^{y_2}\left(\frac{\partial u_y}{\partial z}\frac{\partial u_z}{\partial x}-\frac{\partial u_x}{\partial z}\frac{\partial u_z}{\partial y}\right)\mathrm{d}x\,\mathrm{d}y. \tag{A2}$$

The first two integrals in Eq. (A2) can be combined into a single closed contour integral on ∂A_z. Furthermore, substituting $\omega_x=\frac{\partial u_z}{\partial y}-\frac{\partial u_y}{\partial z}$ and $\omega_y=\frac{\partial u_x}{\partial z}-\frac{\partial u_z}{\partial x}$ in the final double integral in Eq. (A2) reveals that the integral is simply the negative of the tilting term in Eq. (3). As a result, the spanwise convective flux can be rewritten as Eq. (4).

APPENDIX B: THE VORTICITY TILTING TRANSPORT TERM EXPRESSED AS A CONTOUR INTEGRAL

The area integral in the Coriolis tilting term in Eqs. (3) and (4) can be changed to a contour integral by application of Green's theorem. To cast the term in a form resembling that of the OPCF, the reference frame rotation rate can be expressed in terms of the apparent velocity field induced by the solid-body-rotation of the non-inertial reference frame: $\mathbf{u}'=\boldsymbol{\Omega}\times\mathbf{r}$ such that

$$\begin{aligned}\int_{A_z}2\left(\Omega_x\frac{\partial u_z}{\partial x}+\Omega_y\frac{\partial u_z}{\partial y}\right)dA&=2\oint_{\partial A_z}\left(-\Omega_y u_z\,dx+\Omega_x u_z\,dy\right),\\&=-2\oint_{\partial A_z}\left(\frac{\partial u_x'}{\partial z}u_z\,dx+\frac{\partial u_y'}{\partial z}u_z\,dy\right),\\&=-2\oint_{\partial A_z}u_z\frac{\partial}{\partial z}(\mathbf{u}'\cdot\mathbf{ds}).\end{aligned} \tag{B1}$$

REFERENCES

[1]H. Himmelskamp, *Profile Investigations on a Rotating Airscrew*, Reports and Translations Vol. 832 (Aerodynamische Versuchsanstalt, Göttingen, 1947).
[2]J. L. Tangler, "Insight into wind turbine stall and post-stall aerodynamics," Wind Energy **7**, 247–260 (2004).
[3]D. Lentink and M. H. Dickinson, "Biofluiddynamic scaling of flapping, spinning and translating fins and wings," J. Exp. Biol. **212**, 2691–2704 (2009).
[4]K. Mulleners, K. Kindler, and M. Raffel, "Dynamic stall on a fully equipped helicopter model," Aerosp. Sci. Technol. **19**, 72–76 (2012).
[5]J. D. Eldredge and A. R. Jones, "Leading-edge vortices: Mechanics and modeling," Annu. Rev. Fluid Mech. **51**, 75–104 (2019).
[6]M. H. Dickinson, F.-O. Lehmann, and S. P. Sane, "Wing rotation and the aerodynamic basis of insect flight," Science **284**, 1954–1960 (1999).
[7]T. Jardin and L. David, "Spanwise gradients in flow speed help stabilize leading-edge vortices on revolving wings," Phys. Rev. E **90**, 013011 (2014).
[8]C. Giner-Morency and J. G. Wong, "A species-transport model for circulation in a leading-edge vortex," Adv. Aerodyn. **4**, 36 (2022).
[9]L. Feng, Z. Li, and Y. Chen, "Lift enhancement strategy and mechanism for a plunging airfoil based on vortex control," Phys. Fluids **32**, 087116 (2020).
[10]K. Jia, T. Scofield, M. Wei, and S. Bhattacharya, "Vorticity transfer in a leading-edge vortex due to controlled spanwise bending," Phys. Rev. Fluids **6**, 024703 (2021).
[11]T. Maxworthy, "Experiments on the Weis-Fogh mechanism of lift generation by insects in hovering flight. Part 1: Dynamics of the 'fling'," J. Fluid Mech. **93**, 47–63 (1979).
[12]C. P. Ellington, C. van den Berg, A. P. Willmott, and A. L. Thomas, "Leading-edge vortices in insect flight," Nature **384**, 626–630 (1996).
[13]L. Chen, B. Cheng, and J. Wu, "Vorticity dynamics and stability of the leading-edge vortex on revolving wings," Phys. Fluids **35**, 091301 (2023).
[14]C. W. P. Ford and H. Babinsky, "Lift and the leading-edge vortex," J. Fluid Mech. **720**, 280–313 (2013).
[15]T. Jardin, J. Choi, and T. Colonius, "An empirical correlation between lift and the properties of leading-edge vortices," Theor. Comput. Fluid Dyn. **35**, 437 (2021).
[16]D. Lentink and M. H. Dickinson, "Rotational accelerations stabilize leading edge vortices on revolving fly wings," J. Exp. Biol. **212**, 2705–2719 (2009).
[17]D. J. Garmann, M. R. Visbal, and P. D. Orkwis, "Three-dimensional flow structure and aerodynamic loading on a revolving wing," Phys. Fluids **25**, 034101 (2013).
[18]T. Jardin, "Coriolis effect and the attachment of the leading edge vortex," J. Fluid Mech. **820**, 312–340 (2017).
[19]T. Jardin and T. Colonius, "On the lift-optimal aspect ratio of a revolving wing at low Reynolds number," J. R. Soc., Interface **15**, 20170933 (2018).
[20]T. Linehan and K. Mohseni, "On the maintenance of an attached leading-edge vortex via model bird alula," J. Fluid Mech. **897**, A17 (2020).
[21]X. Jia and K. Mohseni, "A theory on leading-edge vortex stabilization by spanwise flow," J. Fluid Mech. **970**, R1 (2023).
[22]J. G. Wong, J. Kriegseis, and D. E. Rival, "An investigation into vortex growth and stabilization for two-dimensional plunging and flapping plates with varying sweep," J. Fluids Struct. **43**, 231–243 (2013).
[23]J. G. Wong, B. P. Labastide, and D. E. Rival, "Flow separation on flapping and rotating profiles with spanwise gradients," Bioinspiration Biomimetics **12**, 026008 (2017).
[24]J. M. Birch and M. H. Dickinson, "Spanwise flow and the attachment of the leading-edge vortex on insect wings," Nature **412**, 729–733 (2001).
[25]L. Chen, J. Wu, and B. Cheng, "Leading-edge vortex formation and transient lift generation on a revolving wing at low Reynolds number," Aerosp. Sci. Technol. **97**, 105589 (2020).
[26]C. J. Wojcik and J. H. J. Buchholz, "Vorticity transport in the leading-edge vortex on a rotating blade," J. Fluid Mech. **743**, 249–261 (2014).
[27]K. Onoue and K. S. Breuer, "A scaling for vortex formation on swept and unswept pitching wings," J. Fluid Mech. **832**, 697–720 (2017).
[28]A. E. Panah, J. M. Akkala, and J. H. J. Buchholz, "Vorticity transport and the leading-edge vortex of a plunging airfoil," Exp. Fluids **56**, 160 (2015).
[29]A. Medina and A. R. Jones, "Leading-edge vortex burst on a low-aspect-ratio rotating flat plate," Phys. Rev. Fluids **1**, 044501 (2016).
[30]M. Acharya and M. H. Metwally, "Unsteady pressure field and vorticity production over a pitching airfoil," AIAA J. **30**, 403–411 (1992).
[31]C. Shih and C. Ho, "Vorticity balance and time scales of a two-dimensional airfoil in an unsteady free stream," Phys. Fluids **6**, 710–723 (1994).
[32]J. M. Akkala and J. H. J. Buchholz, "Vorticity transport mechanisms governing the development of leading-edge vortices," J. Fluid Mech. **829**, 512–537 (2017).
[33]N. H. Werner, H. Chung, J. Wang, G. Liu, J. M. Cimbala, H. Dong, and B. Cheng, "Radial planetary vorticity tilting in the leading-edge vortex of revolving wings," Phys. Fluids **31**, 041902 (2019).
[34]K. J. Wabick, K. C. Johnson, R. L. Berdon, B. S. Thurow, and J. Buchholz, "Transient leading-edge vortex development on a rolling wing in uniform flow," J. Fluid Mech. **957**, A23 (2023).
[35]I. Demirdžić and S. Muzaferija, "Finite volume method for stress analysis in complex domains," Int. J. Numer. Methods Eng. **37**, 3751–3766 (1994).
[36]I. Demirdžić and S. Muzaferija, "Numerical method for coupled fluid flow, heat transfer and stress analysis using unstructured moving meshes with cells

of arbitrary topology," Comput. Methods Appl. Mech. Eng. **125**, 235–255 (1995).
[37]M. Bross, C. A. Ozen, and D. Rockwell, "Flow structure on a rotating wing: Effect of steady incident flow," Phys. Fluids **25**, 081901 (2013).
[38]T. Jardin and L. David, "Coriolis effects enhance lift on revolving wings," Phys. Rev. E **91**, 031001 (2015).
[39]J. G. Wong, G. Gillespie, and D. E. Rival, "Circulation redistribution in leading-edge vortices with spanwise flow," AIAA J. **56**, 3857–3862 (2018).
[40]D. Chen, D. Kolomenskiy, R. Onishi, and H. Liu, "Versatile reduced-order model of leading-edge vortices on rotary wings," Phys. Rev. Fluids **3**, 114703 (2018).
[41]C. E. Brown and W. H. Michael, "Effect of leading-edge separation on the lift of a delta wing," J. Aeronaut. Sci. **21**, 690–694 (1954).
[42]L. Chen, L. Wang, C. Zhou, J. Wu, and B. Cheng, "Effects of Reynolds number on leading-edge vortex formation dynamics and stability in revolving wings," J. Fluid Mech. **931**, A13 (2022).